PAPER

Check for updates

Integration of gold nanoparticles into SnS for enhanced peroxidase-like activity and colorimetric detection of ascorbic acid in fruit juice

Chung-Tu-Nhi Truong,[ab] Van-Dung Le, [iD][ac] Van-Dat Doan, [iD][d] Vinh-Thien Tran,[e] Tran Thi Kim Chi,[f] Tran Thi Huong Giang,[f] T. Ngoc-Han Pham,[g] Cao-Hien Nguyen,[h] Nguyen Thi Thanh Tu[i] and Thanh-Danh Nguyen [iD] *[ac]

A gold/tin(II) sulfide (AuNPs/SnS) nanocomposite was developed as an efficient peroxidase-mimicking nanozyme for colorimetric sensing. Uniformly dispersed Au nanoparticles (~12.0 nm) on the SnS surface created a synergistic interface that significantly enhanced catalytic performance compared with individual components. Under optimized conditions, the nanozyme exhibited a strong peroxidase-like response toward the oxidation of 3,3′,5,5′-tetramethylbenzidine (TMB) by H_2O_2, showing excellent linearity (0–1.14 mM, R^2 = 0.9996) and a low detection limit (LOD) of 0.0022 mM. The system was further applied for ascorbic acid (AA) quantification through ox-TMB reduction, achieving a detection limit of 1.94 μM, a quantification limit of 6.48 μM, and recovery values of 99.7–102.3% in commercial fruit juices. Results were in good agreement with HPLC analysis, confirming analytical reliability. This study highlights the AuNPs/SnS nanocomposite as a robust, cost-effective, and sensitive alternative to natural peroxidases for practical food analysis and colorimetric biosensing.

[a]*Institute of Advanced Technology, Vietnam Academy of Science and Technology, 1A, TL29, An Phu Dong Ward, Ho Chi Minh City, Vietnam. E-mail: danh5463bd@yahoo.com; Fax: +84-28-353521093*

[b]*Center for Diseases Control of Ho Chi Minh City (HCDC), 366A Au Dương Lan, District 8, Ho Chi Minh City, Vietnam*

[c]*Graduate University of Science and Technology, Vietnam Academy of Science and Technology, 18 Hoang Quoc Viet, Nghia Do, Hanoi, Vietnam*

[d]*Faculty of Chemical Engineering, Industrial University of Ho Chi Minh City, 12 Nguyen Van Bao, Ho Chi Minh City, Vietnam*

[e]*Faculty of Environment, Ho Chi Minh City University of Natural Resources and Environment, 236B Le Van Sy Street, Tan Binh District, Ho Chi Minh City 700000, Vietnam*

[f]*Institute of Materials Science, Vietnam Academy of Science and Technology, 18 Hoang Quoc 14 Viet, Cau Giay District, Hanoi 11000, Vietnam*

[g]*NTT Hi-Tech Institute, Nguyen Tat Thanh University, Ho Chi Minh City 700000, Vietnam*

[h]*Department of Chemical Technology, Ho Chi Minh City University of Industry and Trade, Ho Chi Minh City 700000, Vietnam*

[i]*Faculty of Applied Technology, Van Lang School of Technology, Van Lang University, Ho Chi Minh City, Vietnam. E-mail: tu.ntt@vlu.edu.vn*

1. Introduction

Natural enzymes, particularly peroxidases, play crucial roles as biocatalysts in diverse applications ranging from environmental monitoring to biomedical diagnostics and food analysis.[1,2] Peroxidases, a subclass of oxidoreductases, catalyze electron transfer reactions typically involving hydrogen peroxide (H_2O_2) as an electron acceptor and chromogenic substrates as donors.[3] Among them, horseradish peroxidase (HRP) has been widely employed due to its excellent catalytic efficiency and substrate specificity.[4] However, the practical use of natural enzymes is often constrained by inherent limitations such as poor thermal and pH stability, high production costs, and limited shelf life.[5,6]

To overcome these challenges, artificial enzyme mimics, commonly known as nanozymes, have emerged as promising alternatives.[7,8] Artificial enzymes are synthetic materials designed to replicate the catalytic functions of their natural counterparts. Among them, nanomaterial-based nanozymes have garnered considerable attention due to their structural tunability, robustness, and cost-effectiveness.[9,10] Various nanomaterials such as Fe_3O_4 NPs,[11,12] Co_3O_4 NPs,[13] AuNPs,[14,15] PtNPs,[16] and doped metal sulfides[17,18] have demonstrated peroxidase-like activity, enabling their integration into biosensors and catalytic systems. Despite their advantages, many nanozymes still exhibit lower catalytic efficiency than natural enzymes, prompting ongoing efforts to improve their performance through the design of hybrid or composite nanostructures. In particular, hybrid nanozymes combining metal nanoparticles with semiconductor or metal sulfide supports have shown enhanced electron transfer and surface activity, offering improved catalytic responses.[18,19] This strategy is particularly useful in colorimetric assays,[20,21] where signal amplification is essential for the sensitive detection of analytes.

Ascorbic acid (AA), or vitamin C, is a vital water-soluble antioxidant involved in numerous redox processes within biological systems.[22] Its physiological importance includes immune modulation, cardiovascular protection, and the

prevention of oxidative stress-related diseases.[23,24] Given its health relevance, accurate and accessible determination of AA levels in food and biological samples is of significant interest. Conventional detection methods, although accurate, often rely on sophisticated instrumentation and trained personnel, limiting their accessibility.[25]

In this study, we report the synthesis of a gold-decorated tin sulfide nanocomposite (AuNPs/SnS) as a novel peroxidase-like nanozyme. The material demonstrates enhanced catalytic activity for the H_2O_2-mediated oxidation of 3,3′,5,5′-tetramethylbenzidine (TMB), resulting in a visible green color change. To our knowledge, this is the first demonstration of an AuNPs/SnS hybrid acting as a peroxidase mimic in a colorimetric platform. Furthermore, the oxidized TMB product (ox-TMB) was applied for the selective and sensitive colorimetric detection of ascorbic acid in fruit juice samples, highlighting the potential of this nanozyme in practical food analysis.

2. Experimental

2.1. Materials

Chemicals such as $HAuCl_3 \cdot 3H_2O$, citric acid, hydrogen peroxide (H_2O_2) and 3,3′,5,5′-tetramethylbenzidine (red-TMB) were obtained from Acros Co. (Belgium). Glucose, maltose, lactose, hydroperoxide, and ascorbic acid were sourced from Merck Co. (Germany). Orange and apple juice samples were purchased from local stores in Ho Chi Minh City, Vietnam. Distilled water was used in all experimental procedures.

2.2. Synthesis of AuNPs/SnS

SnS nanoparticles were synthesized following a previously reported method.[26] Briefly, a thioacetamide (TAA) solution (0.1 M) was added dropwise to a vigorously stirred $SnCl_2$ solution (0.1 M). The reaction mixture was stirred for 1 hour and then left undisturbed at room temperature for 48 hours. A color change from white to black indicated the formation of SnS nanoparticles. The resulting suspension was centrifuged at 3000 rpm for 3 minutes. The supernatant was discarded, and the precipitate was washed five times with 30 mL of ethanol. After ethanol removal, the solid was dried at 50 °C for 2 hours.

The AuNPs/SnS nanocomposites were prepared using a simple two-phase reaction at room temperature, as described in a previous report.[27] In a typical procedure, 5 mL of $HAuCl_4$ solution (0.1–0.4 mM) was mixed with 5 mL of citric acid solution (0.15 mM) in a beaker. Subsequently, 5 mL of synthesized SnS nanoparticle dispersion (0.1 mM) was added to the gold precursor solution. The mixture was stirred for 20 minutes at room temperature to allow for composite formation. The resulting product was collected by centrifugation and washed with deionized water to remove residual reactants.

2.3. Physicochemical characterisations

The surface morphology and elemental composition of the AuNPs/SnS nanocomposite were investigated using a field-emission scanning electron microscope (FE-SEM, Hitachi S-4800) with solid samples. High-resolution transmission

electron microscopy (HRTEM, JEOL JEM-2100) was employed to examine the morphology and particle size distribution of the nanocomposite. For TEM analysis, a drop of the AuNPs/SnS suspension was deposited onto a carbon-coated copper grid and dried prior to measurement. The particle size distribution was analyzed using ImageJ software. Raman spectroscopy (Horiba XploRa Plus) equipped with a 633 nm excitation laser was performed on solid-state samples to study the bonding characteristics and structural interactions between SnS nanoparticles and the AuNPs/SnS composite.

The optical properties of the synthesized materials were analyzed using a UV-visible spectrophotometer (UV-5100, Shanghai Metash Instruments Co., China) in the wavelength range of 300–800 nm. The functional groups present in the nanocomposites were identified by Fourier-transform infrared (FTIR) spectroscopy using a Tensor 27 spectrometer (Bruker, Germany). Prior to measurement, the solid samples were finely ground and mixed with KBr powder to prepare translucent pellets. The crystalline structure of the AuNPs/SnS nanocomposite was examined by X-ray diffraction (XRD) using a Shimadzu 6100 diffractometer (Japan) operated at 40 kV and 30 mA. The diffraction patterns were recorded over a 2θ range of 10°–80° with a step size of 0.02° and a scanning rate of 4° min^{-1}.

The average crystallite size of the AuNPs/SnS nanocomposite was calculated using the Debye–Scherrer equation (eqn (1)):

$$D = \frac{0.9\lambda}{\beta \cos \theta} \tag{1}$$

where D is the mean crystallite size, λ is the X-ray wavelength, β is the full width at half maximum (FWHM) of the diffraction peak, and θ is the Bragg angle.

2.4. Peroxidase-like activity of AuNPs/SnS nanozyme

Based on the reaction between chromogenic substrate red-TMB and H_2O_2, the peroxidase-like activity of AuNPs/SnS was carried out as follows: 30 μL of red-TMB + 0.6 mL of H_2O_2 (0.1 mM) were mixed with the acetate buffer. After that, AuNPs/SnS were added to the solution and UV-vis spectra were traced with the color change of the solution.

The exploration of detection conditions (pH, concentration of nanozyme, concentration of red-TMB, time) was performed by keeping three factors fixed with changing the other. Similarly, nanocatalysts including SnS nanoparticles, and AuNPs were tested in the same conditions in H_2O_2 concentration of 0–0.2 mM. The evaluation was carried out using measurement of UV-vis spectroscopy and absorbance values were determined at 654 nm.

2.5. Detection of hydrogen peroxide

The colorimetric detection of H_2O_2 was carried out in a 5 mL volumetric flask. Specifically, 0.6 mL of H_2O_2 at various concentrations (0–0.4 mM) was mixed with 30 μL of red-TMB (1.5 mM) in 2 mL of buffer solution at pH 4.5. Subsequently, AuNPs/SnS nanocomposites (10 μg mL^{-1}) were added to flask. The reaction mixture was incubated at room temperature for 20

minutes to ensure adequate reaction time. The absorbance of the resulting solution was then measured using a 10 mm quartz cuvette. UV-vis spectra were recorded in the wavelength range of 400–800 nm to evaluate the colorimetric response.

To establish the linear calibration curve, H_2O_2 solutions with varying concentrations (0–0.4 mM) were tested. The correlation coefficient (R) were evaluated using eqn (2), respectively:

$$R = \frac{\sum \left(x_i - \overline{X}\right)\left(y_i - \overline{Y}\right)}{\sqrt{\sum \left(x_i - \overline{X}\right)^2 \sum \left(y_i - \overline{Y}\right)}} \quad (2)$$

An acceptable linearity was defined by a correlation coefficient in the range of $0.99 \leq R^2 \leq 1$.

2.6. Detection of ascorbic acid

2.6.1. Investigation of detection. The AA detection was performed as follows: in a 5 mL volumetric flask, 30 μL of red-TMB (1.5 mM) + 0.6 mL of H_2O_2 (1.14 mmol L^{-1}) + AuNPs/SnS (10 μg mL^{-1}) + 2.0 mL acetate buffer of pH 4.5 along to produce blue color of ox-TMB. Afterward, the various concentrations of AA ranging from 0 to 0.4 mM were added to the blue color solution.

The exploration of detection conditions including time (5–30 min), temperatures (25–45 °C) was performed by keeping three factors fixed with changing the other. The evaluation was carried out using measurement of UV-vis spectroscopy and absorbance values were determined at 654 nm.

2.6.2. Selectivity test. Citric acid, fructose, lactose, cholesterol, sucrose, glucose, acetic acid, oxalic acid, malic acid, tartaric acid that are likely to be found in real samples were examined as potential interferences for the determination of vitamin C. To investigate the specificity of the proposed method, each kind of foreign substance was individually tested.

2.6.3. Method validation and calibration experiments. Linearity range, method detection limit (MDL) and method quantification limit (MQL) and sensitivity values were determined from the analytical curve, which was assembled from average on triplicate measurements. Linearity range was established from least-squares fitting to the experimental fluorescence with a high determination coefficient of $R^2 > 0.9900$.

MDL and MQL were calculated using the standard deviation (SD) approach according to IUPAC definitions, eqn (3) and (4), respectively. A low-concentration sample was analyzed $n = 14$ times to determine the mean ($\overline{x}$) and SD.

$$MDL = 3 \times SD \quad (3)$$

$$MQL = 10 \times SD \quad (4)$$

where,

$$SD = \sqrt{\frac{\sum (x_i - \overline{x})^2}{n - 1}} \quad (5)$$

Accuracy was evaluated by recovery experiments using ascorbic acid spiked at three concentration levels (0.03, 0.05, and 0.09 mM), with four replicates per level.

Precision was evaluated by the repeatability and the intermediate precision components. Repeatability was tested in three levels of concentration 0.06, 0.10, and 0.18 mM with six replicates (intra-day) and nine replicates over three days (inter-day). The repeatability was calculated via relative standard deviation (RSD) by eqn (6).[27]

$$RSD\% = \frac{SD}{\overline{x}} \times 100 \quad (6)$$

The predicted reproducibility (PRSD) was calculated using the Horwitz eqn (6).[28]

$$PRSD\ (\%) = 0.67 \times 2^{1-0.5\log C} = 2 \times C^{-0.15} \quad (7)$$

Horwitz ratio (HorRat) values were used to assess method performance via eqn (8). It is expected that the HorRat be less than 1.0.[28]

$$HorRat = \frac{RSD}{PRSD} \quad (8)$$

2.6.4. Analysis of real samples. For the detection of AA in the real samples, the commercial juice (two orange juices and one apple juice) were purchased in Ho Chi Minh City between September and December 2023 for method validation. Each 50 mL sample was centrifuged at 5000 rpm for 5 minutes, followed by filtration through a 0.45 μm membrane. The first 5 mL of filtrate was discarded, and the remaining solution was used for analysis. For apple juice, 10 mL of the filtrate was diluted to 20 mL before analysis.

For method validation and comparison, accuracy was assessed by comparing the results with HPLC analysis. Mean values and coefficients of variation (CV) from both methods were calculated. Statistical comparison of precision was performed using the F-test, while mean differences were evaluated with the Student's t-test (eqn (9)).

$$t_{exp} = \frac{|\overline{x_1} - \overline{x_2}|}{\sqrt{\frac{S_1^2}{n_1} + \frac{S_2^2}{n_2}}} \quad (9)$$

where: t_{exp} is experiment t-value; S_1 and S_2 are the sample variances; and n_1 and n_2 are the sample sizes for each method.

3. Results and discussion

3.1. Synthesis of AuNPs/SnS nanozyme

The synthetic route of the AuNPs/SnS nanocomposite is illustrated in Fig. 1. SnS nanoparticles were prepared via a reaction between $SnCl_2$ and 0.1 M thioacetamide (TAA). Elemental analysis using energy-dispersive X-ray spectroscopy (EDX) confirmed the presence of tin and sulfur, with characteristic peaks observed at 2.3 and 3.4 keV.[29] The atomic ratio of Sn-to-S
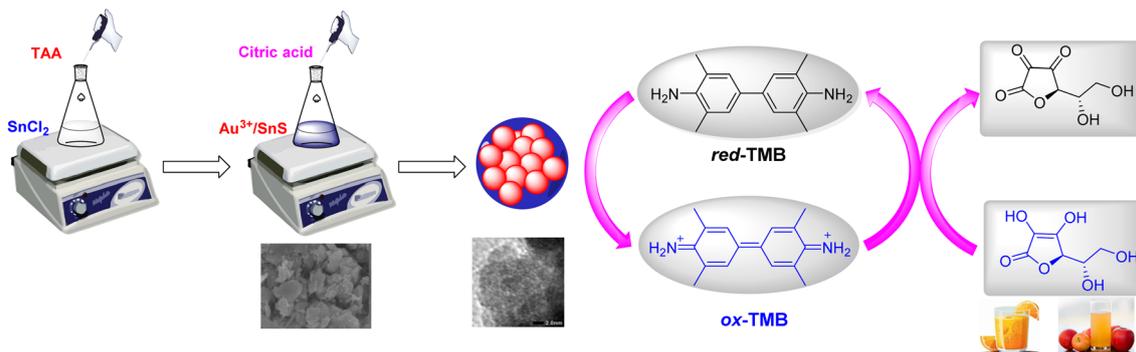
Fig. 1 Schematic illustration of the synthesis of AuNPs/SnS nanoparticles and their peroxidase-mimetic activity for the detection of ascorbic acid.

= 46.7 : 53.3 was close to the expected stoichiometric 1 : 1 ratio, validating successful synthesis.

Following purification, the SnS nanoparticles were combined with AuNPs synthesized *via* citrate reduction of Au^{3+}. Various Au^{3+}/SnS ratios were explored to optimize the physicochemical properties of the resulting nanocomposite. The optimal formulation was subsequently applied for the colorimetric detection of H_2O_2 and ascorbic acid in fruit juice samples.

The physicochemical properties of the AuNPs/SnS nanocomposites with different ratios were systematically investigated using FTIR, Raman spectroscopy, and electron microscopy (SEM and TEM). Raman and FTIR spectra of pristine SnS and AuNPs/SnS nanocomposites are presented in Fig. 2.

X-ray diffraction (XRD) patterns of the nanocomposites with different Au/SnS molar ratios were recorded (Fig. 2A). The pure SnS sample (Au/SnS = 0 : 1) exhibits characteristic diffraction peaks at $2\theta = 26.0°$, $30.4°$, $31.5°$ and $51.1°$, corresponding to the (100), (101), (111), and (112) planes of orthorhombic SnS.[30–32] In

contrast, metallic gold nanoparticles display diffraction peaks at $2\theta = 38.1°$, $44.4°$, $64.8°$, and $77.2°$, indexed to the (111), (200), (220), and (311) planes of face-centered cubic Au.[33,34] For the AuNPs/SnS (1 : 1) sample, only diffraction peaks associated with SnS were observed, indicating either a low loading of AuNPs or a high degree of dispersion that prevented their detection by XRD. At a higher ratio (Au/SnS = 2 : 1), prominent AuNPs peaks appear at $2\theta = 38.1°$, $44.4°$, $64.5°$, and $77.6°$, along with SnS peaks at $2\theta = 27.1°$, $31.9°$, and $52.2°$.[35] In the AuNPs/SnS (3 : 1) and (4 : 1) samples, the Au peaks remain dominant, while only a single SnS peak at $2\theta \approx 52.2°$, assigned to the (112) plane persists. Moreover, these samples showed the broad bands at $14.5°$ and $28.8°$ which are assigned to the residual citric acid (or citrate species) present in the nanocomposite.[36]

These results indicate that increasing the Au content disrupts the crystalline SnS structure, as evidenced by the diminishing intensity of SnS-related peaks in the XRD patterns. The relative peak intensities of Au and SnS increase proportionally with the increasing ratios, suggesting efficient Au^{3+} reduction on the SnS surface. The average crystallite size of the
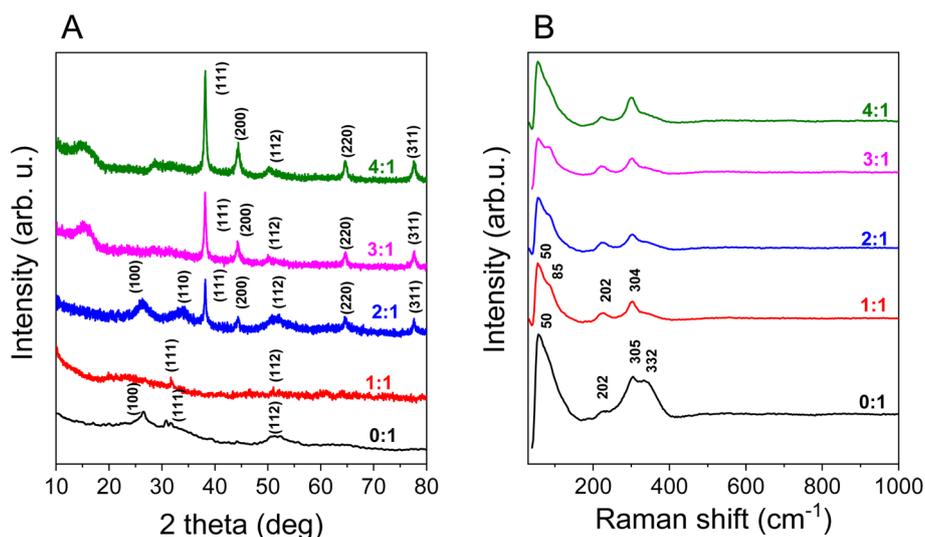

Fig. 2 (A) XRD patterns and (B) Raman spectra of Au/SnS nanocomposites with varying Au-to-SnS ratios: (0 : 1), (1 : 1), (2 : 1), (3 : 1), and (4 : 1).
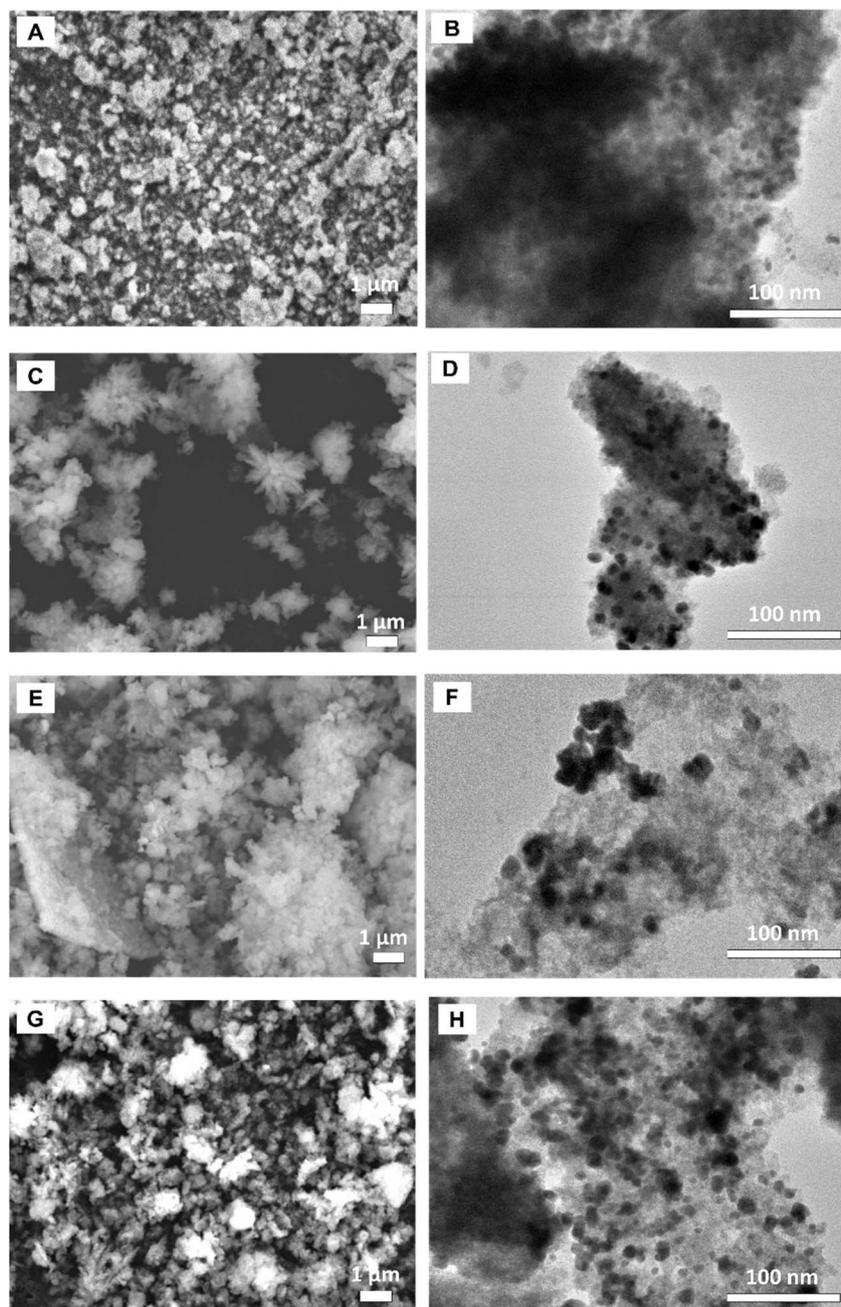
Fig. 3 SEM (left) and TEM (right) images of AuNPs/SnS nanocomposites at different Au-to-SnS ratios: (A and B) AuNPs/SnS 1 : 1; (C and D) AuNPs/SnS (2 : 1); (E and F) AuNPs/SnS (3 : 1); and (G and H) AuNPs/SnS (4 : 1).

AuNPs, estimated from the XRD data using the Scherrer equation, ranges from approximately 24.87 nm, 21.58 nm and 20.38 nm for Au crystals of AuNPs/SnS (2 : 1), (3 : 1) and (4 : 1), respectively (Table S1).

The elemental composition of Au and Sn in the AuNPs/SnS samples was quantitatively analyzed using inductively coupled plasma mass spectrometry (ICP-MS), as summarized in Table S2. The results demonstrated a progressive increase in the Au content with increasing feeding ratios from 1 : 1 to 4 : 1 (Au : Sn). Specifically, the Au content ranged from 0.0108% to 0.4144% (w/w), while the Sn content varied from 63.76% to 74.11% (w/w).

This result explained a low peak intensity of Au crystals in XRD data of sample AuNPs/SnS (1 : 1). Accordingly, the calculated Au-to-Sn weight ratios increased from 0.017 to 0.559 (w/w), confirming the effective incorporation of gold nanoparticles into the SnS matrix as a function of precursor ratio.

To further elucidate the structural evolution, the Raman spectrum of the pure SnS sample exhibits five prominent peaks at 50, 90, 222, 304, and 340 cm^{-1} (Fig. 2A). The peaks located at 50 and 222 cm^{-1} correspond to the characteristic vibrational modes of orthorhombic SnS single crystals. The band at approximately 304 cm^{-1} can be attributed to a secondary tin
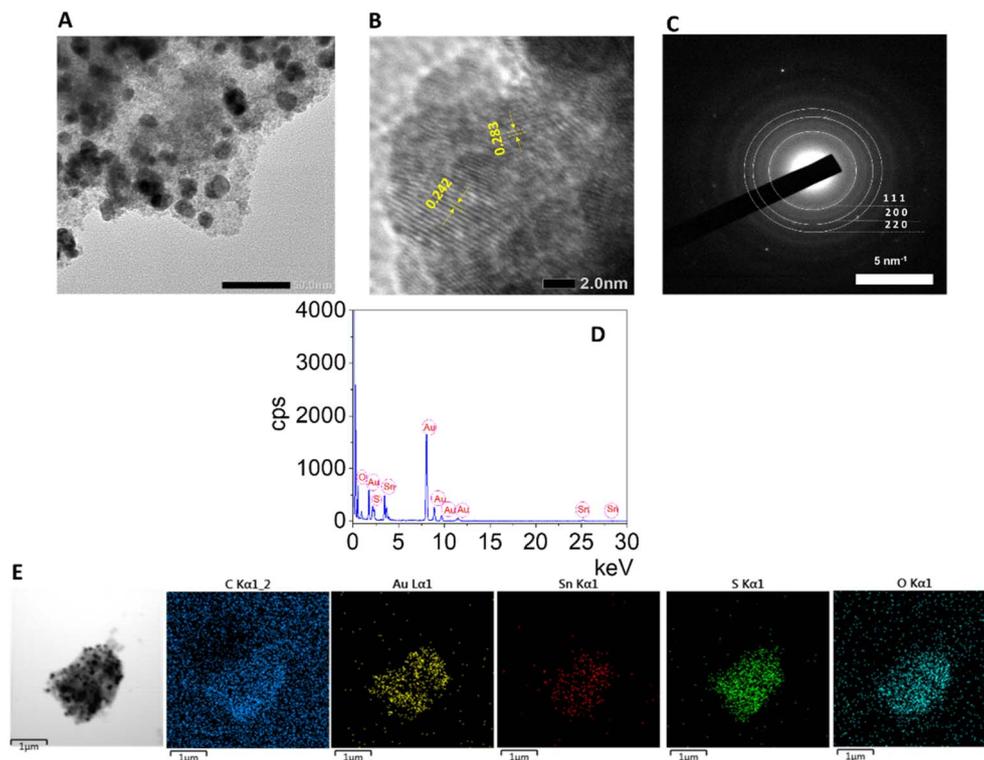
Fig. 4 HRTEM images (A and B), SAED patterns (C), EDX spectrum (D) and STEM − mapping images of AuNPs/SnS (2 : 1) (E).

sulfide phase (Sn_2S_3),[37] whereas the peak near 340 cm^{-1} is associated with zigzag and lattice vibration modes, likely originating from mixed or dimeric structures such as SnS_2 or Sn_2S_2.[38–40] These spectral features suggest that the as-synthesized SnS nanoparticles exhibit a multiphasic nature with diverse Sn–S bonding environments.

Upon the introduction of AuNPs, a marked enhancement in the intensities of the 90 and 222 cm^{-1} peaks is observed, accompanied by a significant reduction in the 332 cm^{-1} peak. This spectral evolution indicates a transition toward a more crystalline and phase-pure SnS structure. The results imply that the presence of AuNPs plays a key role in modulating the crystalline structure by suppressing the multiphasic character and promoting the dominance of single-crystalline SnS domains within the composite matrix.

The surface morphology and particle distribution of AuNPs and SnS were examined using SEM and TEM analyses, as shown in Fig. 3. SEM micrographs (Fig. 3A, C, E and G) reveal that AuNPs are anchored and well-decorated on the SnS surface. At 1 : 1 ratio (Fig. 3A), AuNPs appear sparsely and irregularly distributed, likely due to the low Au loading. In contrast, at a 2 : 1 ratio (Fig. 3C), AuNPs are more uniformly anchored and evenly dispersed across the SnS crystalline domains, suggesting an optimal distribution state. Further increasing the Au content to 3 : 1 and 4 : 1 (Fig. 3E and G) leads to particle aggregation, surface heterogeneity, and partial collapse of the SnS nanostructure, implying excessive incorporation of Au into the matrix. These morphological evolutions are in good agreement with the Raman spectral data, which reveal Au-induced lattice

distortions and structural phase modifications at higher Au loadings.

TEM images (Fig. 3B, D, F and H) further confirm these findings. The dark, high-contrast regions correspond to Au nanoparticles, whereas the lighter background represents the SnS matrix. With increasing Au content, the density of AuNPs increases and their dispersion becomes more continuous, consistent with the SEM observations. Quantitative particle-size analysis reveals a gradual increase in AuNP size from approximately 6.2 nm, 12.0 nm, 13.4 nm and 15.3 nm at the 1 : 1 ratio to the 4 : 1 ratio, respectively indicating that higher Au concentrations promote enhanced nucleation and the AuNPs aggregation with increasing loading ratios. Among the examined samples, the AuNPs/SnS (2 : 1) composite demonstrates the most homogeneous AuNP distribution and minimal structural disruption of the SnS framework, highlighting a balanced integration of metallic and semiconducting phases. This controlled dispersion and preservation of the crystalline structure make AuNPs/SnS (2 : 1) a promising candidate for catalytic and colorimetric applications, particularly in H_2O_2 and ascorbic acid quantification.

The AuNPs/SnS (2 : 1) nanocomposite was subjected to advanced characterization techniques, including high-resolution transmission electron microscopy (HRTEM), selected area electron diffraction (SAED), energy-dispersive X-ray spectroscopy (EDX), and scanning transmission electron microscopy with elemental mapping (STEM-mapping), as shown in Fig. 4. HRTEM images of the AuNPs/SnS (2 : 1) composite (Fig. 3D) clearly display well-defined lattice fringes
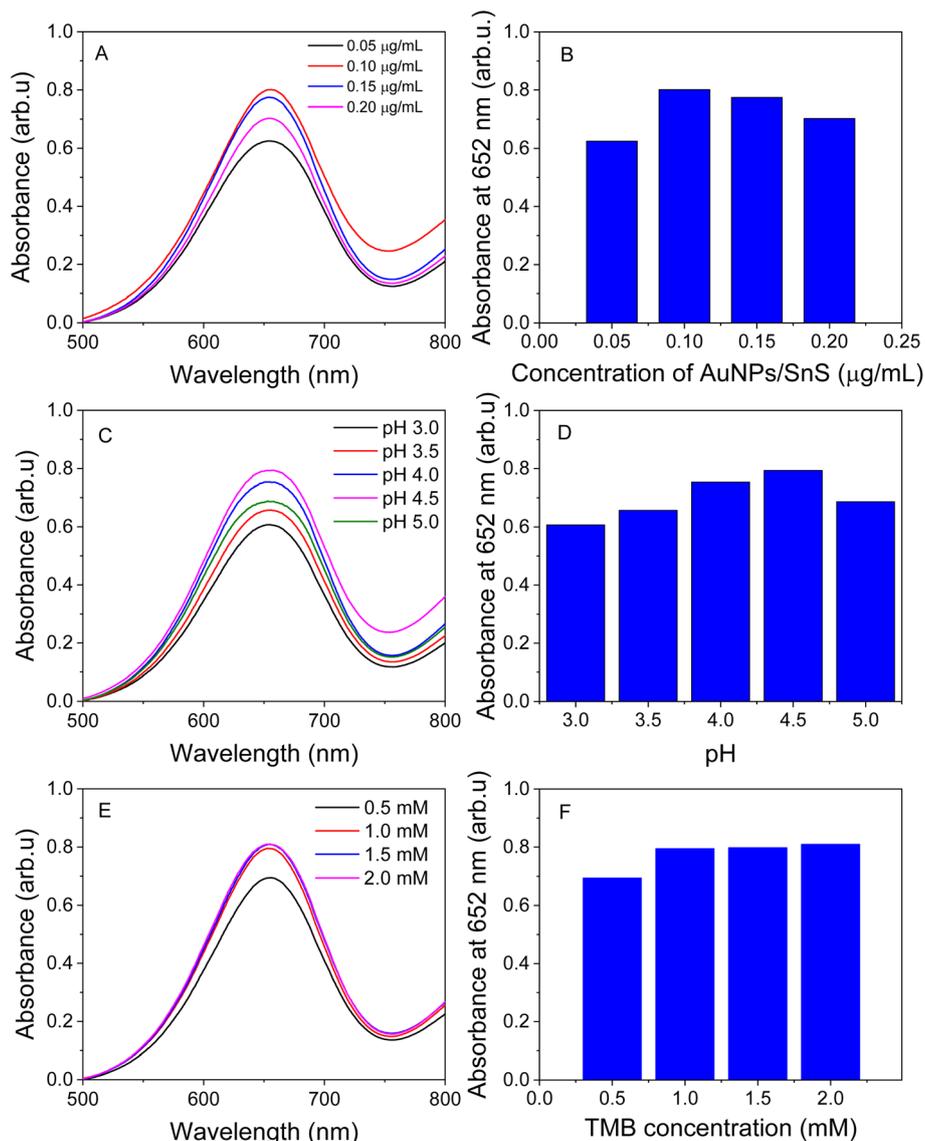
Fig. 5 UV-vis absorption spectra (left) and corresponding absorbance plots at 652 nm (right) for the oxidation of red-TMB using H_2O_2 and catalysis of AuNPs/SnS nanocomposite at the (2 : 1) ratio: (A and B) effect of catalyst concentration; (C and D) effect of pH; (E and F) effect of red-TMB concentration.

with interplanar spacings of 0.242 nm and 0.283 nm, which correspond to the (111) plane of fcc Au and the (111) plane of orthorhombic SnS, respectively.[39,40] The coexistence of these two lattice domains within a single interface suggests a strong structural coherence between AuNPs and the SnS matrix. This alignment indicates that both components preferentially crystallize along the (111) orientation, a configuration widely associated with enhanced structural stability, favorable electron transfer, and improved catalytic activity. Comparable lattice features were also observed in the HRTEM images of the 1 : 1 and 4 : 1 composites (Fig. S2), confirming the persistence of this interfacial crystallographic relationship across different Au loadings.

The SAED pattern further confirmed the crystalline nature of the composite.[41] The observed diffraction rings correspond well to the (111), (200), and (220) planes of metallic Au, consistent with XRD data and affirming the high crystallinity and phase purity of the synthesized nanomaterial.

EDX analysis further verified the elemental composition of the sample, with prominent signals for Au ($\sim$3.0 keV), S ($\sim$2.4 keV), and Sn ($\sim$3.6 and 25.7 keV), confirming the successful incorporation of AuNPs into the SnS matrix.[42] Moreover, elemental mapping through STEM provided spatial distribution maps of Au, Sn, and S, clearly demonstrating the uniform dispersion of AuNPs within the SnS nanoparticles. Collectively, these results confirm that the AuNPs/SnS (2 : 1) sample possesses a well-defined crystalline structure and nanoscale morphology, making it a promising candidate for catalytic applications, particularly in the colorimetric detection of vitamin C *via* the TMB–H_2O_2 reaction system.[43,44]
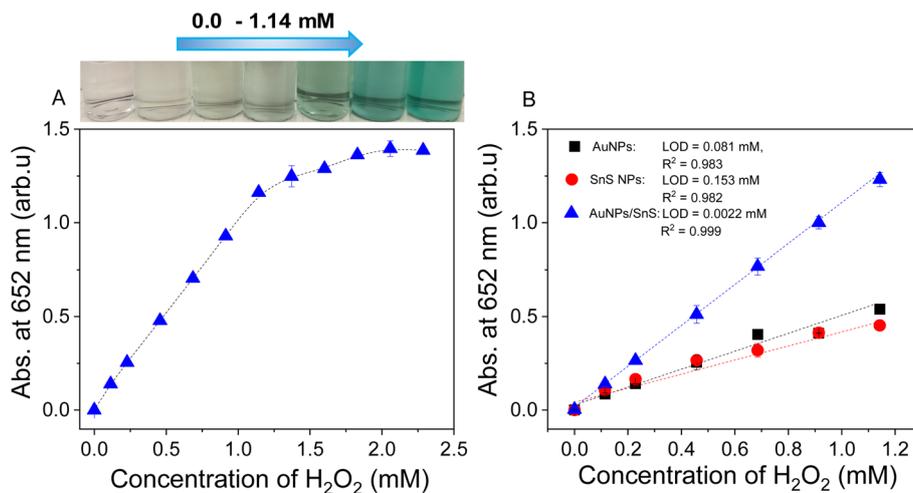
Fig. 6 (A) Calibration curve and (B) linear range for H_2O_2 detection from 0 to 1.14 mM using AuNPs/SnS nanocomposite ratio of (2 : 1).

3.2. Peroxidase-like activity

The oxidation of red-TMB in the presence of AuNPs/SnS nanozyme proceeds *via* a one-electron transfer, generating a stable ox-TMB radical cation through surface-mediated electron transfer. This radical then forms a blue charge-transfer complex with its oxidized diimine form, exhibiting a characteristic absorption peak at 652 nm in the UV-vis spectrum. The proposed mechanism follows a peroxidase-mimicking pathway: (i) H_2O_2 decomposes to generate hydroxyl radicals on the nanozyme surface, and (ii) these radicals subsequently oxidize red-TMB to ox-TMB *via* catalyst surface. Based on this mechanism, several reaction parameters were systematically investigated, including nanozyme concentration, pH, and TMB concentration.

As shown in Fig. 5A and B, the concentration of AuNPs/SnS significantly influenced ox-TMB formation. At 0.05 μg mL^{-1}, the catalyst was insufficient to drive complete oxidation, resulting in low absorbance at 652 nm. The maximum catalytic activity was observed at 0.10 μg mL^{-1}, beyond which (0.15–0.20 μg mL^{-1}), the absorbance decreased, likely due to excess catalyst hindering substrate access or light scattering effects.

The catalytic activity was also found to be pH-dependent (Fig. 5C and D). The absorbance at 652 nm increased with pH, peaking at pH 4.5, and then sharply declined at pH 5.0. These results indicate that mildly acidic conditions (pH 4.5) are optimal for radical generation and stabilization, facilitating effective TMB oxidation.

Fig. 5E and F illustrate the impact of red-TMB concentration on the oxidation efficiency. Increasing the TMB concentration from 0.5 to 1.0 mM led to a proportional rise in absorbance, suggesting enhanced substrate availability. However, further increases to 1.5 and 2.0 mM resulted in minimal changes, indicating that the catalytic system reached saturation at 1.0 mM TMB. Collectively, these results confirm that the optimal conditions for TMB oxidation using AuNPs/SnS nanozyme are: 0.10 μg mL^{-1} catalyst concentration, pH 4.5, and 1.0 mM TMB. These parameters yield the highest absorbance at

652 nm, reflecting efficient formation of the ox-TMB product *via* the peroxidase-like catalytic pathway.

To evaluate the catalytic performance and quantitative detection capability of the AuNPs/SnS nanocomposite, the concentration-dependent response to H_2O_2 was investigated in the range of 0.10–2.30 mM by monitoring the absorbance at 652 nm (Fig. 6A). A distinct linear correlation between absorbance and H_2O_2 concentration was observed within the range of 0.10–1.14 mM, with a color change from colorless to increasingly intense green. The calibration curve exhibited excellent linearity ($R^2 = 0.9996$), following the equation $A = 1.0748 \times [H_2O_2] + 0.016$. At concentrations above 1.14 mM, no significant increase in absorbance was observed, indicating saturation of the catalytic system. Consequently, the quantification was limited to the linear range of 0.10–1.14 mM.

To further assess the synergistic catalytic effect, the performance of the nanocomposite was compared to that of individual AuNPs and SnS NPs under identical conditions (Fig. 6B). The AuNPs and SnS NPs displayed lower linear correlation coefficients ($R^2 = 0.982$ and 0.983, respectively), falling below the acceptable threshold ($R^2 < 0.99$) for reliable quantification. Moreover, the AuNPs/SnS nanocomposite exhibited a markedly lower limit of detection (LOD) of 0.0022 mM, compared to 0.081 mM for AuNPs and 0.153 mM for SnS NPs.

These findings indicate that while AuNPs alone demonstrate superior catalytic activity compared to SnS NPs, their combination in the form of an AuNPs/SnS nanocomposite significantly enhances both sensitivity and linear response. This enhancement is likely attributed to the cooperative interactions between AuNPs and the SnS matrix, which facilitate electron transfer and improve catalytic efficiency in the H_2O_2-mediated oxidation of TMB.

3.3. Quantitative determination of ascorbic acid

3.3.1. Optimization of reaction parameters affecting the reduction of oxidized TMB by ascorbic acid. The influence of temperature and reaction time on the reduction of ox-TMB by
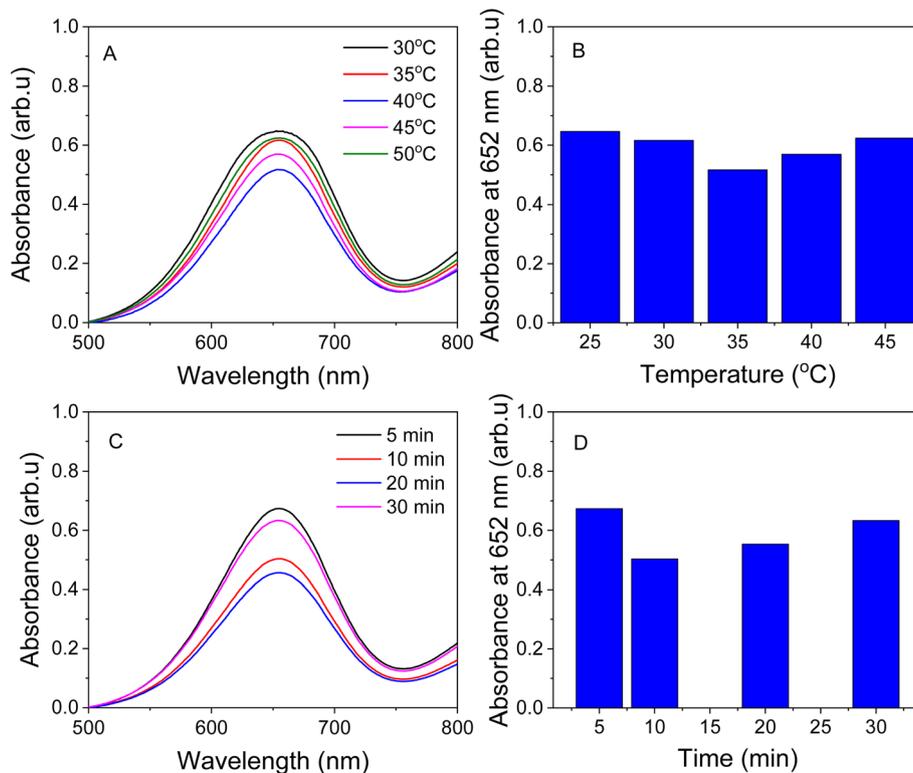
Fig. 7 UV-vis spectra (left) and corresponding plots of absorbance *versus* experimental parameters (right): (A and B) effect of temperature on the reduction of ox-TMB by ascorbic acid; (C and D) effect of reaction time on the reduction efficiency.

AA was systematically examined (Fig. 7). As illustrated in Fig. 7A and B, increasing the temperature from 25 °C to 35 °C resulted in a notable decrease in absorbance at 652 nm, indicating enhanced reduction of ox-TMB by AA. This enhancement is likely due to the promotion of electron transfer kinetics at moderately elevated temperatures. However, further increasing the temperature to 50 °C led to a higher absorbance, suggesting a decline in reductive efficiency. This reduction in activity may be attributed to the thermal instability of AA and/or potential side effects of exothermic reaction conditions that hinder the reduction process. Therefore, 35 °C was selected as the optimal temperature, offering the highest reduction efficiency as reflected by the minimum absorbance observed.

Fig. 7C and D illustrate the effect of reaction time on the reduction process. Over the initial period from 5 to 10 minutes, the absorbance decreased significantly, indicating effective reduction. However, extending the reaction time beyond 10 minutes up to 30 minutes resulted in an increase in absorbance.
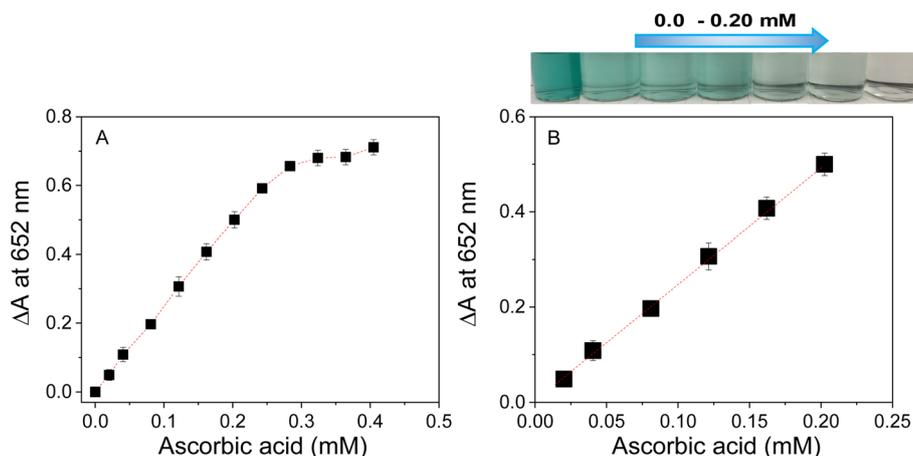

Fig. 8 (A) The effect of varying ascorbic acid concentrations on the absorbance of the ox-TMB system at 652 nm. (B) The corresponding linear calibration curve for ascorbic acid, showing a linear response in the range of 0.02–0.20 mM.

Table 1 Comparison with sensors in literature for AA detection

Probe	Method	Linearity range (μM)	LOD/MDL (μM)	Ref.
Pt-HMCNs	Colorimetric	0.1–200	3.0	45
CoMn NW/NF@C	Colorimetric	0.1–30	4.0	46
Ferric salicylate	Colorimetric	28–400	2.1	47
Pt/CeO$_2$	Colorimetric	0.5–30	8.0	48
Cu$_2$Fe(CN)$_6$@PVP	Colorimetric	10–2000	3.9	49
Ag TNPs	Colorimetric	0–40	2.17	50
Fe$_3$O$_4$@SiO$_2$@Ag	Colorimetric	30–100	10.37	51
PtTi	Electrochemical	200–1000	24.0	52
Au/r-GO/GCE	Electrochemical	240–1500	50.0	53
AuNPs/r-GO	Electrochemical	10–500	3.6	54
bT-ZnO NCs	Electrochemical	4000–28 000	532.1	55
rGO/Fe$_3$O$_4$/GCE	Electrochemical	10–100 000	18.5	56
AuNPs/SnS	Colorimetric	20–200	1.94	This work

This reversal could be due to partial reoxidation of TMB under prolonged exposure to air or thermal degradation of AA over time. Therefore, the optimal reaction condition was determined to be 35 °C with a reaction time of 10 minutes, balancing reduction efficiency and reagent stability.

3.3.2. Method validation. A calibration curve was used to evaluate the linear response range of ox-TMB and AA from 0.020 to 0.40 mM, demonstrating a decrease in absorbance at 652 nm. Based on the change in absorbance (ΔA), a distinct decline was observed from green to colorless with increasing AA concentration in the range of 0.02 to 0.20 mM (Fig. 8). The calibration curve exhibited excellent linearity within this range, with a correlation coefficient (R^2) of 0.999. The corresponding linear regression equation was determined to be $\Delta A = 2.5094 \times [\text{AA}] - 0.0048$. Beyond 0.2 mM up to 0.4 mM, the absorbance change was minimal, indicating a plateau. Therefore, the linear range for AA quantification was established from 0.02 to 0.20 mM.

To determine the method detection limit (MDL) and method quantification limit (MQL) of AA based on the reduction of ox-TMB, the analytical procedure was performed using the standard deviation approach. The experiment was repeated 14 times using a low-concentration sample (0.02 mM) to calculate the mean absorbance and SD. The results are summarized in Table S3. The MDL and MQL were calculated to be 1.94 μM and 6.48 μM, respectively. The reliability factor R was determined to be 9.77 ($R < 10$), confirming that the test solution concentration was appropriate and the calculated MDL is statistically reliable. In this study, the achieved detection limit of 1.94 μM is superior to the other limit of detection (LOD) that reported in previous studies, demonstrating that the newly developed material exhibits promising potential for the determination of AA, as summarized in Table 1.

Recovery was evaluated to assess the accuracy of the method. AA was spiked at three concentration levels (0.0304, 0.0506, and 0.0911 mM), each in quadruplicate. The mean recovery values at each concentration are summarized in Table S4. The HorRat values for all three concentrations were within the acceptable range (HorRat < 1.0), with values of 0.54, 0.30, and 0.40, respectively, indicating acceptable relative standard deviations.[57] The mean recoveries ranged from 99.7% to 102.3%, demonstrating high accuracy within the generally accepted range.[47]

The method repeatability was evaluated at three concentration levels including 60.7, 101.2 and 182.2 μM. All measurements were performed by the same analyst within a single day, with six replicates per concentration. The results yielded HorRat values of 0.423, 0.550, and 0.300, respectively as shown in Table S5. All values were below the threshold of 1.0, indicating that the method meets the acceptability criteria for repeatability. These findings confirm that the method demonstrates satisfactory repeatability across the tested concentration range.

To assess the reproducibility of the method, analyses were conducted at the same three concentration levels (60.7, 101.2, and 182.2 μM) by the same analyst over three different days. Each concentration level was analyzed in triplicate on each day. The relative standard deviations (RSDs) obtained for the low, medium, and high concentrations were 5.00%, 3.63%, and 4.67%, respectively (Table S6). All HorRat values (0.70, 0.50, 0.65) were within acceptable limits (HorRat < 1.0), indicating that the method demonstrates robust inter-day reproducibility.
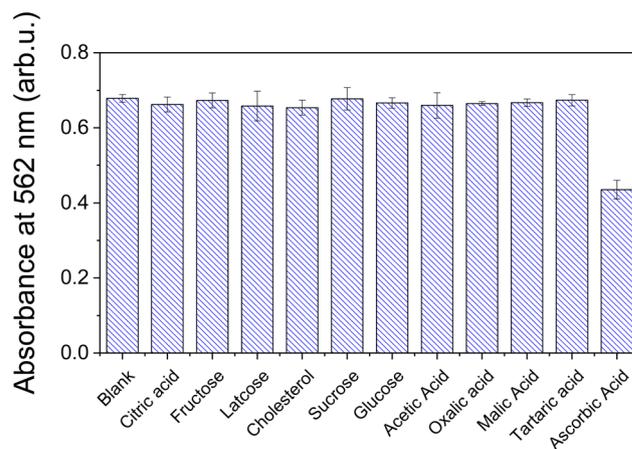

Fig. 9 Selectivity evaluation of the proposed method for ascorbic acid detection in the presence of various potential interfering substances.

Table 2 Analytical results of AA in fruit juice samples and statistical comparison between UV-vis and HPLC methods

Samples	UV-vis (mM)		HPLC (mM)	RSD (%)	Exp. t-value (t_{exp})	Critical t-value (t_c)
	Mean	SD				
Orange juice 1	2.610	0.052	2.589	1.98	1.36	2.571
Orange juice 2	5.478	0.146	5.458	2.67	0.34	
Apple juice	0.765	0.020	0.751	2.66	1.75	

For the selectivity of the method, potential interfering substances were tested under identical analytical conditions used for ascorbic acid detection. These included various organic reductants such as citric acid, fructose, lactose, cholesterol, sucrose, glucose, acetic acid, oxalic acid, malic acid, and tartaric acid. Each experiment was performed in triplicate, and the average absorbance values were recorded. As illustrated in Fig. 9, most of these substances did not cause significant changes in the absorbance intensity, indicating minimal interference. Notably, only cholesterol and lactose exhibited a measurable impact on the TMB reduction reaction, with recovery of 12.4% and 10.6%, respectively. However, in the presence of AA, the absorbance at 652 nm decreased markedly due to the reduction of ox-TMB to its colorless form. These findings demonstrate that the method exhibits high selectivity toward AA, with negligible interference from common coexisting compounds.

3.4. Applications for analysis of ascorbic acid in fruit juices

Three fruit juice samples were pretreated and subsequently analyzed using two different methods: UV-vis spectrophotometry employing ox-TMB prepared by catalysis of AuNPs/SnS, and high-performance liquid chromatography (HPLC), which served as the reference method. To evaluate the repeatability and reproducibility of the UV-vis method, each sample was analyzed in six replicates. The RSD values obtained for orange juice 1, orange juice 2, and apple juice were 1.98%, 2.66%, and 2.61%, respectively, all below 11%, indicating acceptable repeatability and reproducibility (Table 2).

In addition to assessing the reliability of the methods based on RSD values, the accuracy between the two methods was evaluated using a paired t-test. The statistical analysis showed $t_{exp} < t_c$, confirming no significant differences between the results obtained from the UV-vis and HPLC methods. Thus, the results indicated the accuracy and reliability of the UV-vis approach. These findings suggest that the nanocomposite AuNPs/SnS has promising potential as a peroxidase-mimicking catalyst for the oxidation of target compounds and may serve as a viable alternative for food analysis applications.

4. Conclusions

A nanocomposite AuNPs/SnS was successfully synthesized as an efficient peroxidase mimic for the colorimetric detection of H_2O_2 and ascorbic acid. The nanomaterial, consisting of ~12.0 nm Au nanoparticles uniformly distributed on SnS nanoparticles, exhibited enhanced catalytic activity due to the synergistic effect between Au and SnS. The optimal Au-to-SnS ratio (2 : 1) and reaction conditions were determined, and a linear response for H_2O_2 was obtained from 0 to 1.14 mM. The sensor was further applied for ascorbic acid detection in fruit juices, showing a detection limit of 1.92 μM in linearity range of 0.02 to 0.20 mM, excellent recovery (99.74–102.3%), and good precision. Results from three commercial juice samples were consistent with those from the HPLC method, confirming the accuracy and applicability of the AuNPs/SnS-based nanozyme. This study highlights the potential of nanocomposite AuNPs/SnS as stable, cost-effective alternatives to natural peroxidases in food analysis.

Conflicts of interest

The authors declare that they have no conflicts of interest.

Data availability

The data used to support the findings of this study are included within the article. The data supporting this article have been included as part of the supplementary information (SI). Supplementary information is available. See DOI: https://doi.org/10.1039/d5ra05712d.

Acknowledgements

References

1 V. P. Pandey, M. Awasthi, S. Singh, S. Tiwari and U. N. Dwivedi, *Biochem. Anal. Biochem.*, 2017, **6**, 308.

2 C. P. Kurup and M. U. Ahmed, *Biosensors*, 2023, **13**, 461.

3 S. A. Geleto, B. T. Gutema, A. M. Ariti, B. A. Ankala, A. A. Achamyeleh, E. G. Mekonnen, K. N. Mekonnen, Y. A. Workie, E. M. Abda and M. L. Mekonnen, in *Nanozymes*, Elsevier, 2024, pp. 19–44.

4 G. R. Lopes, D. C. Pinto and A. M. Silva, *RSC Adv.*, 2014, **4**, 37244–37265.

5 J. Chapman, A. E. Ismail and C. Z. Dinu, *Catalysts*, 2018, **8**, 238.

6 A. Taheri-Kafrani, S. Kharazmi, M. Nasrollahzadeh, A. Soozanipour, F. Ejeian, P. Etedali, H.-A. Mansouri-Tehrani, A. Razmjou, S. M.-G. Yek and R. S. Varma, *Crit. Rev. Food Sci. Nutr.*, 2021, **61**, 3160–3196.

7 E. Kuah, S. Toh, J. Yee, Q. Ma and Z. Gao, *Chem.–Eur. J.*, 2016, **22**, 8404–8430.

8 N. E. T. Castillo, E. M. Melchor-Martínez, J. S. O. Sierra, N. M. Ramírez-Torres, J. E. Sosa-Hernández, H. M. Iqbal and R. Parra-Saldívar, *Int. J. Biol. Macromol.*, 2021, **179**, 80–89.

9 S. Fedeli, J. Im, S. Gopalakrishnan, J. L. Elia, A. Gupta, D. Kim and V. M. Rotello, *Chem. Soc. Rev.*, 2021, **50**, 13467–13480.

10 S. Singh, N. Rai, H. Tiwari, P. Gupta, A. Verma, R. Kumar, V. Kailashiya, P. Salvi and V. Gautam, *ACS Appl. Bio Mater.*, 2023, **6**, 3577–3599.

11 X. Wang, W. Guo, Y. Hu, J. Wu, H. Wei, X. Wang, W. Guo, Y. Hu, J. Wu and H. Wei, *Nanozymes: Next Wave of Artificial Enzymes*, 2016, pp. 57–91.

12 P. Sudhesh, S. Sruthi, M. Jose, K. Vyshnavi, P. Aiswarya and R. Manu, *Sci. Rep.*, 2025, **15**, 1–14.

13 J. Mughal, H. Ahmad, A. Tariq, M. Mitee Ullah, U. Draz, S. M. Ramay and S. Atiq, *Diamond Relat. Mater.*, 2024, **150**, 111736.

14 F. Mancin, L. J. Prins, P. Pengo, L. Pasquato, P. Tecilla and P. Scrimin, *Molecules*, 2016, **21**, 1014.

15 Z. Zhang, L. M. Bragg, M. R. Servos and J. Liu, *Chin. Chem. Lett.*, 2019, **30**, 1655–1658.

16 J. Jia, X. Du, X. Lv, F. Xie, J. Zhou and J. Cai, *ACS Appl. Nano Mater.*, 2023, **6**, 15224–15233.

17 W. Fu, K. Zhang, X. Zhang, G. Fan, Z. Wang, S. Chen, Y. Wen and P. Wang, *Electrochim. Acta*, 2023, **437**, 141535.

18 Y. Zhang, R. Li, X. Li, P. Zheng, W. Zhu, C. Nie and Q. Pan, *ACS Appl. Nano Mater.*, 2025, **8**(22), 11521–11556.

19 L. Feng, S. Song, H. Li, R. He, S. Chen, J. Wang, G. Zhao and X. Zhao, *Metals*, 2023, **13**, 792.

20 M. Lian, M. Liu, X. Zhang, W. Zhang, J. Zhao, X. Zhou and D. Chen, *ACS Appl. Mater. Interfaces*, 2021, **13**, 53599–53609.

21 J. Zhu, X. Peng, W. Nie, Y. Wang, J. Gao, W. Wen, J. N. Selvaraj, X. Zhang and S. Wang, *Biosens. Bioelectron.*, 2019, **141**, 111450.

22 E. Agwu, C. Ezihe and G. Kaigama, in *Ascorbic Acid – Biochemistry and Functions*, IntechOpen, 2023.

23 A. Gęgotek and E. Skrzydlewska, *Antioxidants*, 2022, **11**, 1993.

24 A. Alberts, E.-T. Moldoveanu, A.-G. Niculescu and A. M. Grumezescu, *Molecules*, 2025, **30**, 748.

25 M. R. Gartia, S. K. Misra, M. Ye, A. Schwartz-Duval, L. Plucinski, X. Zhou, D. Kellner, L. T. Labriola and D. Pan, *Sci. Rep.*, 2015, **5**, 16011.

26 G. Zhang, Z. Fu, Y. Wang and H. Wang, *Adv. Powder Technol.*, 2015, **26**, 1183–1190.

27 W. Horwitz and R. Albert, *J. AOAC Int.*, 2006, **89**, 1095–1109.

28 AOAC International, *AOAC Official Method Anal.*, AOAC Int., 2016, pp. 1–18.

29 S. Hegde, P. Murahari, B. J. Fernandes, R. Venkatesh and K. Ramesh, *J. Alloys Compd.*, 2020, **820**, 153116.

30 J. Henry, K. Mohanraj, S. Kannan, S. Barathan and G. Sivakumar, *J. Exp. Nanosci.*, 2015, **10**, 78–85.

31 X.-L. Gou, J. Chen and P.-W. Shen, *Mater. Chem. Phys.*, 2005, **93**, 557–566.

32 D. Alagarasan, S. Varadharajaperumal, K. D. A. Kumar, R. Naik, S. Umrao, M. Shkir, S. AIFaify and R. Ganesan, *Opt. Mater.*, 2021, **121**, 111489.

33 F. J. Kadhum, S. A. Aziz and H. T. Sulaiman, *J. Phys.: Conf. Ser.*, 2025, **2974**(1), 012023.

34 S. Sathiyaraj, G. Suriyakala, A. D. Gandhi, R. Babujanarthanam, K. S. Almaary, T.-W. Chen and K. Kaviyarasu, *J. Infect. Public Health*, 2021, **14**, 1842–1847.

35 T. T. N. Nguyen, T. T. Vo, B. N. H. Nguyen, D. T. Nguyen, V. S. Dang, C. H. Dang and T. D. Nguyen, *Environ. Sci. Pollut. Res.*, 2018, **25**(34), 34247–34261.

36 R. O. Toro, Doctor thesis, Universitat Politècnica de València, Valencia, 2015.

37 S. H. Chaki, M. D. Chaudhary and M. P. Deshpande, *Adv. Nat. Sci.: Nanosci. Nanotechnol.*, 2014, **5**, 045010.

38 U. Chalapathi, B. Poornaprakash, W. J. Choi and S.-H. Park, *Appl. Phys. A: Mater. Sci. Process.*, 2020, **126**, 583.

39 I. Yonemori, S. Dutta, K. Nagashio and K. Wakabayashi, *AIP Adv.*, 2021, **11**, 095106.

40 S. Sohila, M. Rajalakshmi, C. Ghosh, A. Arora and C. Muthamizhchelvan, *J. Alloys Compd.*, 2011, **509**, 5843–5847.

41 T. M.-T. Nguyen, T. A.-T. Nguyen, N. Tuong-Van Pham, Q.-V. Ly, T. T.-Q. Tran, T.-D. Thach, C.-L. Nguyen, K.-S. Banh, V.-D. Le and L.-P. Nguyen, *Arabian J. Chem.*, 2021, **14**, 103096.

42 A. S. ALmomani, A. F. Omar, A. A. Oglat, S. S. Al-Mafarjy, M. A. Dheyab and T. H. Khazaalah, *S. Afr. J. Chem. Eng.*, 2025, **53**, 142–152.

43 M. K. Masud, S. Yadav, M. N. Islam, N.-T. Nguyen, C. Salomon, R. Kline, H. R. Alamri, Z. A. Alothman, Y. Yamauchi and M. S. A. Hossain, *Anal. Chem.*, 2017, **89**, 11005–11013.

44 S. Siddiqui, J. Niazi and A. Qureshi, *Mater. Today Chem.*, 2021, **22**, 100560.

45 H. Chen, C. Yuan, X. Yang, X. Cheng, A. A. Elzatahry, A. Alghamdi, J. Su, X. He and Y. Deng, *ACS Appl. Nano Mater.*, 2020, **3**, 4586–4598.

46 M. Lu, B. Li, L. Guan, K. Li and Y. Lin, *ACS Sustain. Chem. Eng.*, 2019, **7**, 15471–15478.

47 S. F. El-Malla, F. R. Mansour, R. H. Elattar and A. H. Kamal, *J. AOAC Int.*, 2023, **106**, 276–284.

48 X. Liu, X. Wang, C. Qi, Q. Han, W. Xiao, S. Cai, C. Wang and R. Yang, *Appl. Surf. Sci.*, 2019, **479**, 532–539.

49 X. Zhang, X. Zhou, Q. Wan, T. Sun and G. Gao, *Talanta*, 2025, **293**, 128152.

50 W. Qiao, Y. Liu, X. Fan, Y. Yang, W. Liu, L. Wang, Z. Hu, F. Liu, C. Jin and X. Sun, *Curr. Res. Food Sci.*, 2023, **7**, 100548.

51 M. A. Tarighat, F. H. Ghorghosheh and G. Abdi, *Mater. Sci. Eng., B*, 2022, **283**, 115855.

52 D. Zhao, G. Yu, K. Tian and C. Xu, *Biosens. Bioelectron.*, 2016, **82**, 119–126.

53 C. Wang, J. Du, H. Wang, C. e. Zou, F. Jiang, P. Yang and Y. Du, *Sens. Actuators, B*, 2014, **204**, 302–309.

54 F. Mazzara, B. Patella, G. Aiello, A. O'Riordan, C. Torino, A. Vilasi and R. Inguanta, *Electrochim. Acta*, 2021, **388**, 138652.

55 P. Singh, K. R. Singh, J. Singh, P. Prasad and R. P. Singh, *RSC Adv.*, 2021, **11**, 25752–25763.

56 J. Niranjana, H. Koyakutty, A. A. Thomas and M. J. Bushiri, *Mater. Sci. Eng., B*, 2023, **290**, 116283.

57 V. Paez, W. B. Barrett, X. Deng, C. Diaz-Amigo, K. Fiedler, C. Fuerer, G. L. Hostetler, P. Johnson, G. Joseph and E. J. Konings, *J. AOAC Int.*, 2016, **99**, 1122–1124.